Submesoscale Rossby waves on the Antarctic circumpolar current

John R. Taylor, Scott Bachman, Megan Stamper, Phil Hosegood, Katherine A. Adams, Jean-Baptiste Sallée, Ricardo Torres

OCEANOGRAPHY

Submesoscale Rossby waves on the Antarctic circumpolar current

John R. Taylor,[1]* Scott Bachman,[2] Megan Stamper,[1] Phil Hosegood,[3] Katherine Adams,[4] Jean-Baptiste Sallee,[5] Ricardo Torres[6]

The eastward-flowing Antarctic circumpolar current (ACC) plays a central role in the global ocean overturning circulation and facilitates the exchange of water between the ocean surface and interior. Submesoscale eddies and fronts with scales between 1 and 10 km are regularly observed in the upper ocean and are associated with strong vertical circulations and enhanced stratification. Despite their importance in other locations, comparatively little is known about submesoscales in the Southern Ocean. We present results from new observations, models, and theories showing that submesoscales are qualitatively changed by the strong jet associated with the ACC in the Scotia Sea, east of Drake Passage. Growing submesoscale disturbances develop along a dense filament and are transformed into submesoscale Rossby waves, which propagate upstream relative to the eastward jet. Unlike their counterparts in slower currents, the submesoscale Rossby waves do not destroy the underlying frontal structure. The development of submesoscale instabilities leads to strong net subduction of water associated with a dense outcropping filament, and later, the submesoscale Rossby waves are associated with intense vertical circulations.

INTRODUCTION

The Antarctic circumpolar current (ACC) transports water between the major ocean basins and forms the linchpin of the global meridional overturning circulation (*1*). The ACC is composed of a series of interconnected jets, each associated with abrupt changes in density, or fronts. The Subantarctic Front (SAF) and Polar Front (PF) are the strongest climatological fronts associated with the ACC. Here, deep density surfaces (or isopycnals) outcrop to the sea surface, providing a pathway along which water can upwell to the ocean surface, exchange heat, carbon, and oxygen with the atmosphere, and return to the ocean interior (*2*). The Southern Ocean is a significant sink for anthropogenic carbon and heat (*3*, *4*). Southern Ocean fronts and their associated jets and eddies also represent a potential source of energy to drive enhanced submesoscale activity. Although submesoscales are active in the Southern Ocean (*5*, *6*), their structure and dynamics have not been fully characterized.

OBSERVATIONS

The first attempt to directly observe the three-dimensional structure of submesoscales in the Southern Ocean was made as part of the Surface Mixed Layer Evolution at Submesoscales (SMILES) project from 18 April 2015 to 22 May 2015 in a region east of Drake Passage in the Scotia Sea. During the cruise, a large northward meander of the SAF (Fig. 1A) was sampled at high resolution using towed bodies, a ship-mounted acoustic Doppler current profiler, and surface drifters. The meander was first surveyed with 25 sections between 25 and 40 km in length made with a towed SeaSoar instrument during a time when the meander broke off to form an isolated mesoscale eddy (*7*). A transect through the northern edge of the meander made on 9 May, before the eddy formation process, shows two opposing fronts surrounding a cold, dense filament (Fig. 1B). The "outer" front is associated with a very sharp temperature contrast, which is partially compensated by salinity. The "inner" front with a smaller temperature change is associated with a larger density gradient.

The cold filament and its associated fronts are embedded in a very fast current flowing clockwise around the meander. The current is nearly depth-independent over the upper 200 m. The top panel in Fig. 1B shows the velocity projected onto the direction perpendicular to the section and averaged in the upper 200 m. We will refer to this as the ACC jet. Although the ACC jet is wider than the fronts that it contains, the vertical component of the relative vorticity is large, ranging from $-0.4f$ to $0.5f$, where f is the local Coriolis frequency.

High-resolution satellite imagery on 11 May indicates the presence of submesoscale meanders of the sharp temperature gradient associated with the developing meander (Fig. 1A). Qualitatively similar features have been observed before, notably along the Gulf Stream, where they have been called "shingles" and "tongues" (*8*, *9*). Here, the observed features have wavelengths of 5 to 15 km and are embedded in a broad current with speeds in excess of 1 m s^{-1}, making them difficult to observe with traditional methods due to the fast time scales associated with their advection. Immediately after completing a Seasoar survey of the newly formed eddy, we repeatedly sampled a fixed line across the fronts with the towed moving vessel profiler (MVP) (Fig. 1A). The winds were relatively weak during the Seasoar section and at the start of the MVP survey (with wind stress, $\tau < 0.1$ N/m^2), although the wind became strong at the end of the MVP survey ($\tau \simeq 0.25$ N/m^2). A time series of the wind stress and direction is shown in the Supplementary Materials.

The MVP observations confirmed the presence of submesoscale meanders along the sharp temperature front. To visualize the approximate three-dimensional structure of the temperature field, we adopt a frozen field hypothesis and convert the time of each section into an "advected distance" by multiplying the time elapsed since the first section by a constant velocity characteristic of the depth-averaged velocity in the mixed layer (1.2 m s^{-1}). The result, shown in Fig. 1C, suggests that the meanders have a spacing of 5 to 15 km. The meanders extend to the base of the mixed layer (120 to 160 m), with evidence of intrusions of cold water crossing to the warm side of the thermal front.

[1]Department of Applied Mathematics and Theoretical Physics, University of Cambridge, Centre for Mathematical Sciences, Wilberforce Road, Cambridge, UK. [2]National Center for Atmospheric Research, Boulder, CO 80307, USA. [3]School of Biological and Marine Sciences, Plymouth University, Plymouth, UK. [4]Scripps Institution of Oceanography, University of California, San Diego, La Jolla, CA 92093, USA. [5]Sorbonne Universités, Université Pierre et Marie Curie (UPMC)/CNRS, Laboratoire d'Océanographie et du Climat Numériques (LOCEAN) Laboratory, Paris, France. [6]Plymouth Marine Laboratory, Plymouth, UK.
*Corresponding author. Email: j.r.taylor@damtp.cam.ac.uk

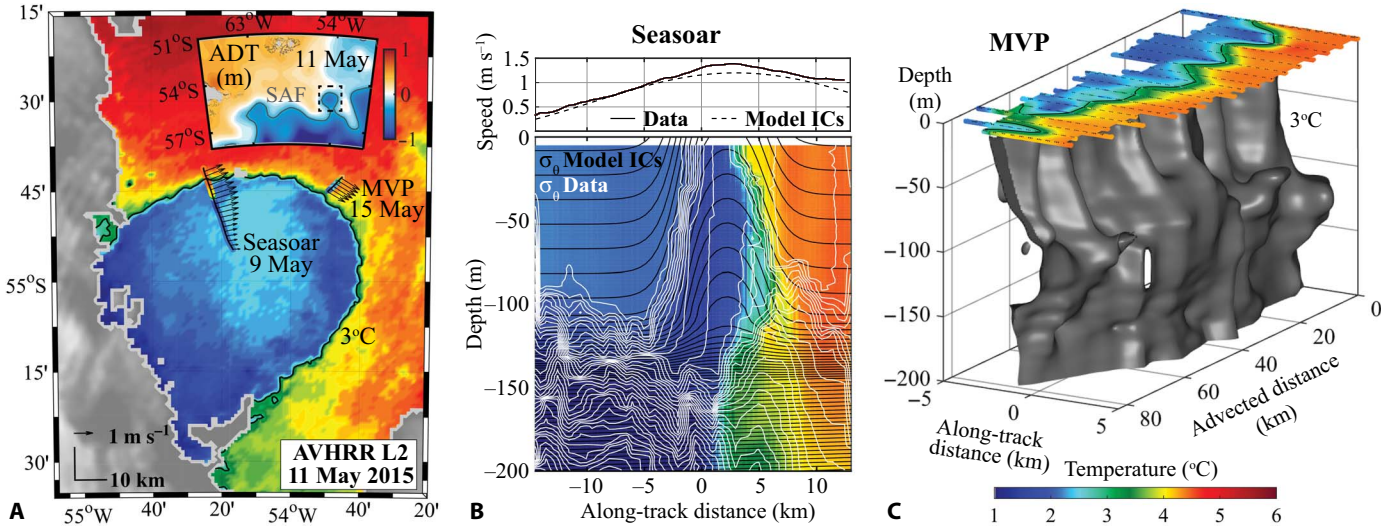

Fig. 1. SeaSoar section and MVP survey. (**A**) Map of survey site with temperature (color, main panel) and Absolute Dynamic Topography (ADT), and locations of the Seasoar section and MVP survey with surface temperature (colored dots) and surface velocity vectors. (**B**) Seasoar section from 9 May with depth-averaged along-front current speed (top) and temperature and potential density (bottom, color shading and white contours). The corresponding model initial conditions (ICs) are also shown. The potential density contour interval is 0.01 kg m^{-1}. (**C**) MVP survey conducted on 15 May at the location indicated in (A). The time of each section is converted to advected distance by multiplying the approximate speed of the ACC jet (1.2 m/s). The top surface shows temperature from the MVP, averaged above a depth of 20 m (shading), and from the ship's flow-through intake (colored dots). The 3°C isotherm is interpolated into along-track, advected distance, and depth coordinates and displayed as a gray isosurface.

These observations raise a number of intriguing questions. For example, are the submesoscale meanders generated locally through an instability of the filament or fronts, and if so, what is the source of their energy? Why do the meanders appear very close to the center of the ACC jet, and how does the jet influence their formation and evolution? Do the submesoscale currents enhance subduction of surface water? We will address these questions here.

FRONTAL INSTABILITY

To address the first of the questions listed above, we analyzed the linear stability of an idealized representation of the observed density and velocity, which forms the "basic state." The idealized density section (black contours, Fig. 1B, bottom) consists of two opposing fronts in a 100-m-deep mixed layer. Below the mixed layer is a pycnocline with a weaker horizontal density gradient and a large vertical stratification. The velocity is taken to be in thermal wind balance with the density field, with the addition of a broad ACC jet perpendicular to the buoyancy gradient with a sinusoidal shape, a wavelength of 50 km, and a maximum velocity of 1.2 m s^{-1} (dashed line, Fig. 1B, top). The idealized section is assumed to be independent of the along-stream direction (parallel to the ACC jet), and the curvature of the front is neglected. Further details of the idealized section are given in the Supplementary Materials.

The Seasoar section (Fig. 1B) has small regions with $fq < 0$, where $q \equiv (f\hat{\mathbf{k}} + \boldsymbol{\zeta}) \cdot \nabla b$ is the potential vorticity, f is the Coriolis parameter, $\hat{\mathbf{k}}$ is the local vertical unit vector, $\boldsymbol{\zeta} = \nabla \times \mathbf{u}$ is the relative vorticity, and b is the fluid buoyancy. As a result, conditions at the fronts are favorable for symmetric instability (*10*, *11*). However, the motion associated with symmetric instability is, by definition, independent of the along-front direction (*12*), and hence, symmetric instability is unlikely to cause the observed meanders. To restrict our analysis to other possible instabilities, we exclude symmetric instability by adding a constant stratification to the basic state with a buoyancy frequency of $N_0 = 2.5 \times 10^{-3}$ s^{-1}, which is sufficient to ensure $fq > 0$.

Despite the idealizations introduced above, the stability analysis is still complicated by the fact that the basic state is two-dimensional with variation in the cross-stream and vertical directions, rendering the equations describing the evolution of linear perturbations nonseparable. To overcome this problem, we use a time-stepping method to isolate the most unstable features. The velocity and density are first decomposed into background and perturbation components

$$\mathbf{u}(x,y,z,t) = \bar{u}(y,z)\hat{\mathbf{i}} + \mathbf{u}'(x,y,z,t),$$
$$\rho(x,y,z,t) = \bar{\rho}(y,z) + \rho'(x,y,z,t) \quad (1)$$

where x, y, and z denote the along-stream, cross-stream, and vertical directions, and the overbar denotes the background state. We further decompose the perturbation variables using a Fourier transform, for example

$$\mathrm{u}'(x,y,z,t) = \hat{u}(k,y,z,t)e^{ikx} \quad (2)$$

where $\hat{}$ denotes the complex amplitude associated with along-stream wave number, k. Because linear perturbations evolve independently, each Fourier mode can be solved separately. We timestep the equations describing the evolution of the complex amplitude until the fastest growing instability is isolated with a constant exponential growth rate. Further details of this method are provided in the Supplementary Materials.

The most unstable features develop along the outer front with an along-front wavelength of about 12.5 km (Fig. 2A). This is consistent with the observed spacing between meanders and supports the hypothesis that these features are generated through a submesoscale instability. The kinetic energy associated with the most unstable perturbations grows via the buoyancy flux (solid red line, Fig. 2A), indicative of mixed layer instability (MLI), an ageostrophic baroclinic instability (*13*). The

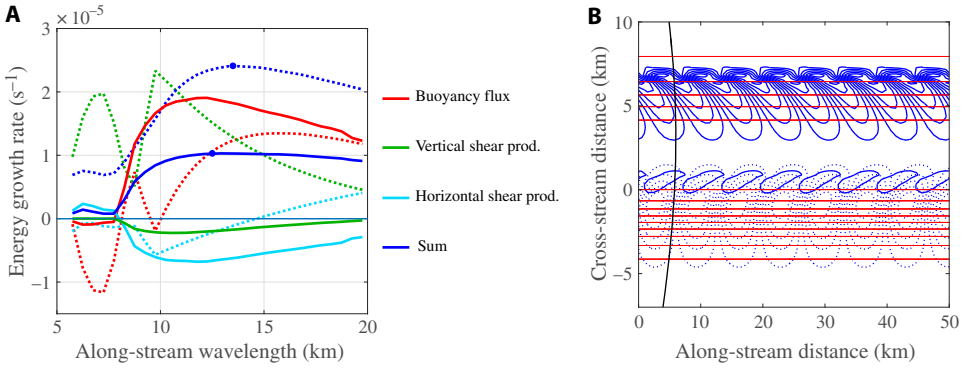

Fig. 2. Linear stability analysis of the model initial conditions shown in Fig. 1B. (**A**) Perturbation energy source terms for a basic state with (solid) and without (dotted) the ACC jet. Blue dots indicate the most unstable mode. (**B**) Density perturbations associated with the most unstable mode with (solid blue) and without (dotted blue) the ACC jet. Surface density contours (red) and the ACC jet profile (black) are also shown.

horizontal and vertical shear production remove energy from the most unstable perturbations and transfer energy to the mean flow, thereby reducing the growth rate. The negative horizontal shear production is also associated with an up-gradient flux of momentum toward the center of the ACC jet. Suppression of baroclinic instability by horizontally sheared barotropic flow has been noted before and has been termed the "barotropic governor" (*14*). The barotropic governor is less effective at the outer front where the horizontal shear is smaller than at the inner front, explaining why the instabilities at the outer front grow faster, despite the fact that the outer front is weaker than the inner front.

The ACC jet not only influences the growth rate associated with MLI but also controls which front is the most unstable. To show this, we repeated the linear stability analysis without the ACC jet included in the basic state. When the ACC jet is removed, the growth rate associated with the fastest growing mode increases by a factor of 2.3 as the vertical shear production becomes a significant source (Fig. 2A). Notably, without the ACC jet, the most unstable mode shifts from the outer front to the inner front, where the horizontal density gradient is larger (Fig. 2A).

NONLINEAR EVOLUTION

To examine the nonlinear evolution of the submesoscale instabilities and their influence on the evolution of the fronts, we used fully nonlinear, nonhydrostatic numerical simulations starting with the same idealized initial conditions described above. The model domain was 50 km in both horizontal directions and 200 m in the vertical direction. The flow is uniform in the along-stream (x) direction. The simulations use free-slip, adiabatic, rigid-lid boundary conditions at the top and bottom of the domain and are therefore unforced by wind or surface heating/cooling. Gridpoints were uniformly spaced with a resolution of about 100 m in the horizontal directions and 1 m in the vertical direction. Unresolved motions were parameterized with constant Laplacian viscosity and diffusivity with coefficients of 0.3 $m^2\ s^{-1}$ and $3 \times 10^{-5}\ m^2\ s^{-1}$ in the horizontal and vertical directions, respectively. Growing modes are seeded using random perturbations with an amplitude of 1 $mm\ s^{-1}$.

As in the linear stability analysis, we ran simulations with and without the ACC jet. Without the ACC jet, a submesoscale instability first develops along the inner front with an along-stream wavelength of about 12.5 km, consistent with the location and scale of the most unstable mode predicted from the linear stability analysis. After about 10 days of simulation time, four distinct cyclonic submesoscale eddies develop. These eddies interact and fill the domain with a field of submesoscale fronts and eddies after 30 days of model time (Fig. 3A, upper left inset).

The nonlinear evolution of the submesoscale instabilities is markedly different in the presence of the ACC jet. Here, a submesoscale instability first develops along the outer front. After 30 days of model time, the submesoscale wave rolls up into a billow-like structure (Fig. 3A, upper right inset) before an instability develops on the inner front. Later, 60 days after initializing the model, the submesoscales interact nonlinearly and lead to a state with temperature filaments and eddies on a broader range of scales (Fig. 3A, lower right inset). The zonal frontal structure remains intact in this case.

The relative distortion of the temperature front can be quantified by calculating the equivalent contour length

$$L_{eq}(T,t) = \left[\frac{\frac{\partial}{\partial A}\iint |\nabla_h T|^2 dA}{(\partial T/\partial A)^2}\right]^{1/2} \quad (3)$$

where $A(T, t)$ is the horizontal surface area occupied by water with temperature less than T and ∇_h is the horizontal gradient operator (*15*, *16*). Here, we define $\bar{L}_{eq}$ as the average of L_{eq} over the temperature range $3^\circ C \le T \le 4.5^\circ C$ and compare this with $\bar{L}_0$, the value of $\bar{L}_{eq}$ associated with the initial conditions. In both simulations, $\bar{L}_{eq}$ increases as submesoscale instabilities develop and distort the temperature contours, and in both cases, the growth of $\bar{L}_{eq}$ saturates after 25 to 30 days (note that the long spin-up time is partly due to the small amplitude of the disturbances used to initialize the models.) When the ACC jet is present, $\bar{L}_{eq} < 5L_0$, significantly smaller than in the simulation without the ACC jet (Fig. 3A). For comparison, when normalized by the length of an undisturbed temperature contour, the MVP observations give $\bar{L}_{eq} \simeq 1.5\bar{L}_0$. This is somewhat smaller but generally within 1 standard deviation of the prediction from the model with a jet when subsampled at the approximate resolution of the observations. In contrast, without an ACC jet, the saturated value of $\bar{L}_{eq}$ is more than 20 times larger than L_0.

SUBMESOSCALE ROSSBY WAVES

The ACC jet transforms the developing instabilities into submesoscale Rossby waves. Upstream phase propagation is evident in the model at the center of the outer front (Fig. 3B). The phase propagation is consistent with Rossby waves supported by the local gradient of

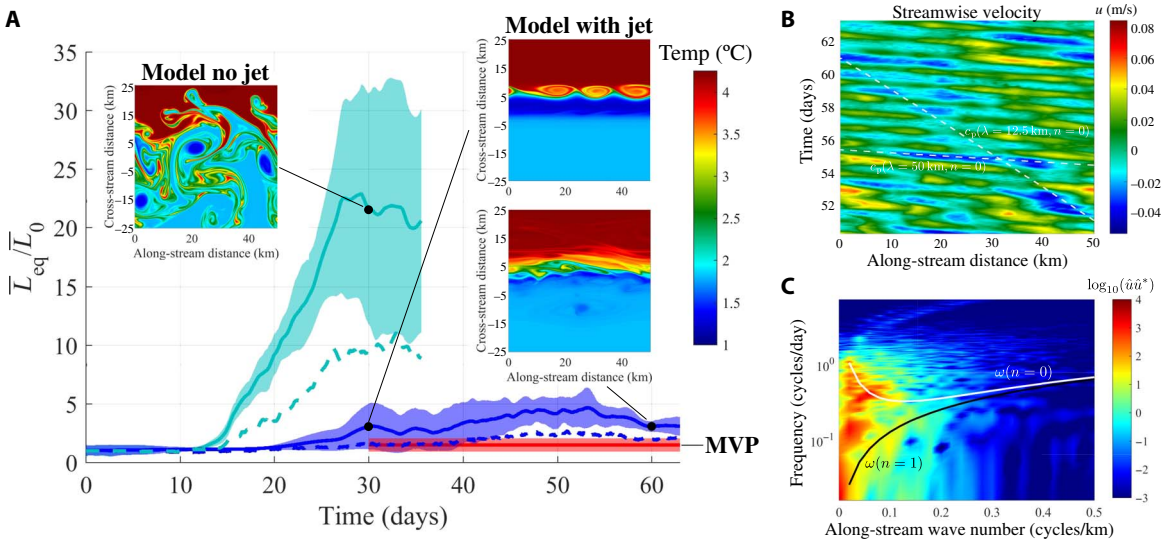

Fig. 3. Nonlinear numerical simulations. (**A**) Equivalent temperature contour length, L_{eq}, as defined in Eq. 3, normalized by its minimum value, L_0, and averaged from 3° to 4.5°C (solid lines). Shaded regions indicate ±1 SD about the average over the temperature range. Dashed lines indicate the mean value of L_{eq} from each model, subsampled (with a resolution of 4 km × 400 m) to approximate the spacing of the MVP measurements. Insets show the temperature at a depth of 50 m. (**B**) Space-time diagram of the streamwise velocity at a depth of 50 m and a cross-stream distance of 4.25 km for the late stages of the model simulation with a jet included. Note that the velocity associated with the ACC jet at this location has been subtracted from u. White dashed lines have a slope equal to the phase speed calculated from Eq. 4 with the indicated along-stream wavelengths and independent of the cross-stream direction. (**C**) Power spectrum associated with the along-stream velocity at the same cross-stream distance as in (B), calculated for the full duration of the model with an ACC jet. Solid white and black lines indicate the dispersion relation from Eq. 4 for mixed layer baroclinic modes (n = 1) and barotropic modes (n = 0). In both cases, the cross-stream wave number is set to zero.

potential vorticity. Although the velocity and density in the model are nontrivial functions of depth and cross-stream distance, a simple dispersion relation for quasi-geostrophic Rossby waves can be written by assuming that stratification is constant in the mixed layer, the mixed layer base is rigid, and the Rossby number is small

$$\omega = kc_p = \bar{u}k + \frac{-\beta + \bar{u}_{yy}}{|\mathbf{k}|^2 + \frac{n^2\pi^2}{R_{ML}^2}} \quad (4)$$

where ω and c_p are the frequency and phase velocity, n is the vertical mode number, $R_{ML} = N_{ML}H_{ML}/f_0$ is the mixed layer deformation radius, and N_{ML} and H_{ML} are the buoyancy frequency and depth associated with the mixed layer. The power spectrum of the cross-stream velocity, calculated along the center of the front, shows distinct peaks coinciding with the dispersion relation for barotropic (n = 0) and mode 1 mixed layer baroclinic (n = 1) Rossby waves. Note that dispersion curves for deeper baroclinic modes with penetration into the thermocline lie between the indicated lines.

DOWNWELLING

Comparing the horizontal slices of temperature at a depth of 50 m from the model with an ACC jet, it is evident that the water associated with the cold filament (defined by temperatures < 1.5°C) occupies less horizontal surface area after 60 days of model time than at 30 days or the initial state (Fig. 3A, right insets). The observations also suggest active subduction of the filament water. For example, comparing the Seasoar section (Fig. 1B) with a composite of the later MVP sections (Fig. 4A) reveals that the filament water that was seen at the surface in the Seasoar section is only seen near the base of the mixed layer in the MVP survey. An along-stream average of the temperature from the model reproduces the slumping of the cold filament (compare Fig. 4, A and B), which then spreads out at the base of the mixed layer. Note that the very cold water appearing in the bottom left of Fig. 4A was not included in the model initial conditions, where temperature was initially depth-independent with a minimum value of about 1.2°C. In the model, the water that began in the filament forms periodic intrusions of cold water on the warm side of the outer front, qualitatively similar to those seen in Fig. 1C. Because the initial condition was in thermal wind balance and the model does not include surface forcing or mesoscale eddies, subduction in the model can be directly linked to submesoscale activity.

In the later stages of the model simulation, the submesoscale Rossby waves are associated with intense vertical circulations. The *rms* vertical velocity and mean density, calculated using an along-stream (x) average at a depth of 50 m, are shown in Fig. 5 (A and B). In the model without the ACC jet (Fig. 5A), the *rms* vertical velocity reaches a maximum value of approximately 50 m day^{-1} as instabilities develop at the inner front, a value consistent with previous models of submesoscale flows (*17*–*19*). When the ACC jet is included in the model, the *rms* vertical velocity is significantly larger (approximately 100 m day^{-1}), and large *rms* vertical velocities are maintained until the end of the simulation. The simulation also exhibits a strong internal gravity wave field, which leads to large *rms* vertical velocities on the flanks of the jet.

The submesoscale instabilities drive subduction of the cold, dense filament initially found between the inner and outer fronts. The total volume of water with potential density $\sigma_\theta > 26.95$ kg m^{-3} passing through a horizontal plane at a depth of 50 m is similar for both simulations (Fig. 5C), although with the ACC jet the rate of subduction is weaker ($\simeq$ 6500 m^3/s) but more sustained than in the absence of the ACC jet. Subduction eventually ends once the dense filament sinks to the base of the mixed layer (Fig. 4), which is a consequence of the unforced simulations in a periodic horizontal domain. In reality, resupply of dense water to the filament or vertical mixing in response to intermittent

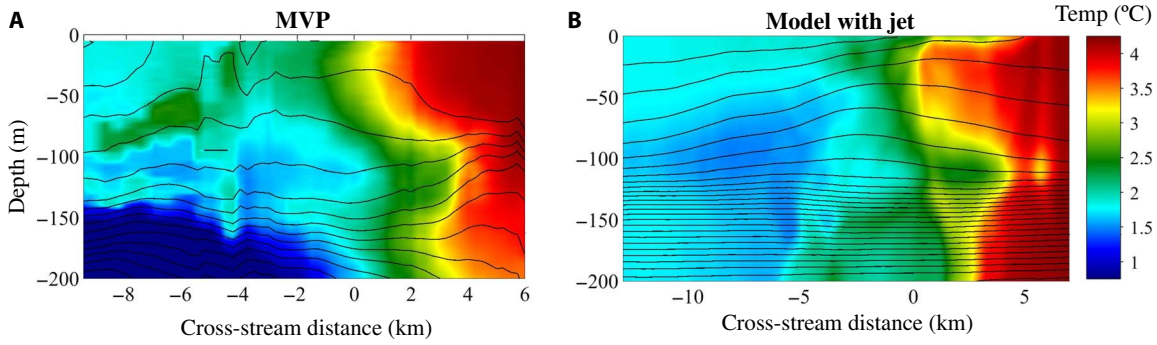

Fig. 4. Average temperature and density sections. (**A**) Composite temperature (color) and density (black contours), averaged for all MVP sections. (**B**) Along-stream (*x*) averaged temperature (color) and density (black contours) from the model with the ACC jet at 53 days. The initial temperature was independent of depth in the model.

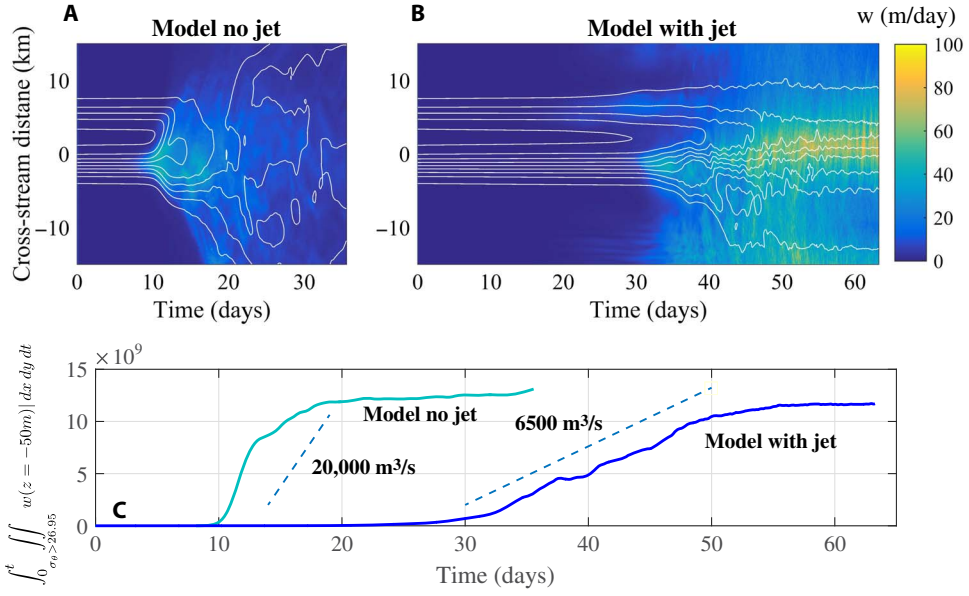

Fig. 5. Vertical velocity and subduction. *rms* vertical velocity at $z = 50$ m depth with respect to an average in the *x* direction, from the model without (**A**) and with (**B**) the ACC jet. White contour lines show *x*-averaged density with a contour interval of 0.01 kg m^{-1}. Volume of water with potential density $\sigma_\theta > 26.95$ kg/m^3 subducted below $z = -50$ m. The slope of the dashed lines corresponds to the labeled volumetric subduction rate.

storm events could sustain subduction. Note that the subduction rate decreases by about a factor of 10 if we exclude the inner front from the model initial conditions (see the Supplementary Materials), although the qualitative features of the simulations with and without ACC jets remain very similar.

IMPLICATIONS

The results presented here indicate that the strong currents associated with the ACC confine locally generated submesoscale disturbances to the core of the ACC jet and support submesoscale Rossby waves. In the absence of wind, surface cooling, or large-scale confluence, net subduction of water in a dense filament occurs during the development of submesoscale instabilities. Following the equilibration of submesoscale instabilities and development of submesoscale Rossby waves, the net subduction rate slows but large localized vertical velocities persist near the center of the ACC jet (Fig. 5, B and C).

Extrapolating the subduction rate from the model to the entire length of the ACC suggests that submesoscales might make a significant contribution to the total subduction in this region (see calculation in the Supplementary Materials). Note that large subduction rates and strong vertical circulations also develop in the model with the same frontal structure but without the ACC jet. This is consistent with the recent work of Bachman *et al.* (*20*) who found localized patches of large submesoscale eddy kinetic energy throughout the Scotia Sea. However, in the simulations that include the ACC jet, submesoscale activity and the associated vertical velocity are enhanced in a relatively narrow region near the jet core (see Fig. 5B). This suggests that the strong currents present in the ACC have the potential to confine the most intense subduction events associated with submesoscales to a relatively small area.

The largest subduction rate in the model occurs during the development of submesoscale motions when the dense, outcropping filament sinks to the base of the mixed layer. Persistent subduction of water in a specific density class would require a mechanism to resupply surface water in this density class to fronts or filaments along the ACC. Our simulations do not show a significant change in the volume associated with each density class (see the Supplementary Materials), suggesting that another process is needed. Net advection of dense surface water

toward the front and water mass transformation are two candidates. Our simulations exclude net advection toward the front due to the periodic boundary conditions. Wind and air-sea heat fluxes are likely important factors in contributing to water mass transformation, and both of these processes were excluded from the simulations.

The subduction of mode water, which occurs north of the SAF in the Scotia Sea (*2*, *21*), is intimately linked to the Southern Ocean sink of anthropogenic heat and carbon (*3*, *4*, *22*). Although our observations were limited in time and space, high-resolution numerical models could help to quantify the influence of submesoscales on water mass subduction along the ACC fronts. Submesoscale processes are not presently resolved in climate models, and quantifying their associated subduction rates has the potential to improve estimates of the ocean uptake of heat and carbon.

The fronts associated with the ACC are known to act as barriers to lateral mixing (*23*, *24*), although much of the past work in this area has not directly considered the influence of submesoscales. Here, we find that the ACC jet restricts submesoscale activity to the center of the front and supports submesoscale Rossby waves, and the front is much less distorted by submesoscales than it would be if the jet were absent. The large reduction in equivalent temperature contour length (Fig. 3A) implies a strong reduction in the effective horizontal diffusivity associated with stirring by submesoscale motions (*25*). Regional variations in the confinement of submesoscales at ACC fronts could modulate lateral mixing rates in the Southern Ocean. This could have important implications for the exchange of surface waters between the Southern Ocean and the surrounding ocean basins.

Submesoscales have been shown to enhance primary production by upwelling nutrient-rich water into the euphotic layer (*26*, *27*) and reducing light limitation (*28*–*30*). Although chlorophyll concentrations in the Southern Ocean are generally low, elevated concentrations have been observed near major fronts (*31*). The influence of submesoscale physics on primary production in the Southern Ocean is not well understood, but future observational campaigns and modeling studies could help quantify this influence. In particular, the very large vertical velocities reported here (Fig. 5B) could stimulate primary production along the front by bringing nutrients up into the euphotic layer (*32*).

One of the remarkable features of the simulation with a strong ACC jet is the coherence of the front at the end of the model simulation. The linear stability analysis shows that the ACC jet reduces the growth rate of submesoscale instabilities, but it does not fully stabilize the flow. The mechanisms behind the jet-induced equilibration of the front remain unknown. Building a dynamical description of this process will be important to predicting properties of the fully developed system including the frontal width and the size of the submesoscale eddies. This will also be an important step in extrapolating the results presented here to other regions of the global ocean.

MATERIALS AND METHODS

Numerical simulations

The numerical simulations used a code developed and described by Taylor (*33*). The code solved the nonhydrostatic, incompressible, Boussinesq equations. The numerical method combined a pseudo-spectral method in both horizontal directions with a second-order accurate centered finite difference method in the vertical direction. The time-stepping algorithm used a mixed third-order accurate Runge-Kutta scheme and Crank-Nicolson for the viscous/diffusive terms. The nonhydrostatic pressure was treated using the projection method of Karniadakis *et al.* (*34*). The 2/3 de-aliasing method (*35*) was used to prevent spurious aliasing associated with the Fourier transform applied to the nonlinear advection terms. The initial conditions are described in detail in the Supplementary Materials.

Linear stability analysis

The linear stability analysis reported in Fig. 2 was performed by time-stepping the linearized governing equations. A two-dimensional basic state was first prescribed using the initial conditions described in the Supplementary Materials. The basic state varies only in the cross-front (y) and vertical (z) directions. All fields were decomposed into departures from the basic state, for example, $u = \bar{u}(y, z) + u'(x, y, z, t)$. The equations for departures from the basic state (for example, u') were then linearized, assuming small departures from the basic state (for example, $u' << \bar{u}$). A Fourier transform was then applied in the along-front (x) direction to yield a set of equations for the complex Fourier amplitudes [for example, $\hat{u}(k, y, z, t)$]. A set of discrete along-front wave numbers (k) was chosen. For each wave number, the linearized equations for the Fourier amplitudes were time-stepped until the exponential growth (or decay) rate reached a steady state. At the start of each time-stepping loop, the Fourier amplitudes were seeded with a set of random perturbations with uniform amplitude in Fourier space.

The numerical method used in the linear stability solver was similar to that used in the fully nonlinear simulations, except that second-order centered finite differences were used to calculate derivatives in the y and z directions. The time-stepping method used the same third-order accurate Runge-Kutta/Crank Nicolson method as in the nonlinear simulations, and the projection method was used to calculate the nonhydrostatic pressure.

SUPPLEMENTARY MATERIALS

Supplementary material for this article is available at http://advances.sciencemag.org/cgi/content/full/4/3/eaao2824/DC1

Observations

Numerical simulations

Model initial conditions

Subduction estimate

fig. S1. Wind stress (N/m^2) and wind angle (degrees from east) calculated using the algorithm of Large and Pond (*36*).

fig. S2. Profiles of the buoyancy (blue), temperature (red), and depth-averaged velocity (green) associated with the model initial conditions and the linear stability analysis.

fig. S3. Probability density functions of potential density at the end of each simulation.

fig. S4. Subducted volume (units of m^3) for the simulations reported in the main text with two opposing fronts surrounding a dense filament and two additional simulations with just the outer front present.

References (*37*–*41*)

REFERENCES AND NOTES

1. J. Marshall, K. Speer, Closure of the meridional overturning circulation through Southern Ocean upwelling. *Nat. Geosci.* **5**, 171–180 (2012).
2. J.-B. Sallée, K. Speer, S. Rintoul, S. Wijffels, Southern Ocean thermocline ventilation. *J. Phys. Oceanogr.* **40**, 509–529 (2010).
3. T. L. Frölicher, J. L. Sarmiento, D. J. Paynter, J. P. Dunne, J. P. Krasting, M. Winton, Dominance of the Southern Ocean in anthropogenic carbon and heat uptake in CMIP5 models. *J. Climate* **28**, 862–886 (2015).
4. S. Khatiwala, F. Primeau, T. Hall, Reconstruction of the history of anthropogenic CO_2 concentrations in the ocean. *Nature* **462**, 346–349 (2009).
5. I. Rosso, A. M. Hogg, A. E. Kiss, B. Gayen, Topographic influence on submesoscale dynamics in the Southern Ocean. *Geophys. Res. Lett.* **42**, 1139–1147 (2015).
6. C. B. Rocha, T. K. Chereskin, S. T. Gille, D. Menemenlis, Mesoscale to submesoscale wavenumber spectra in Drake Passage. *J. Phys. Oceanogr.* **46**, 601–620 (2016).
7. K. A. Adams, P. Hosegood, J. R. Taylor, J.-B. Sallée, S. Bachman, R. Torres, M. Stamper, Frontal circulation and submesoscale variability during the formation of a Southern Ocean mesoscale eddy. *J. Phys. Oceanogr.* **47**, 1737–1753 (2017).

8. W. von Arx, D. Bumpus, W. Richardson, On the fine-structure of the Gulf Stream front. *Deep Sea Res.* **3**, 46–65 (1955).
9. F. Webster, A description of Gulf Stream meanders off Onslow Bay. *Deep Sea Res.* **8**, 130–143 (1961).
10. D. A. Bennetts, B. J. Hoskins, Conditional symmetric instability—A possible explanation for frontal rainbands. *Q. J. R. Meteorol. Soc.* **105**, 945–962 (1979).
11. J. R. Taylor, R. Ferrari, On the equilibration of a symmetrically unstable front via a secondary shear instability. *J. Fluid Mech.* **622**, 103–113 (2009).
12. P. H. Stone, On non-geostrophic baroclinic stability. *J. Atmos. Sci.* **23**, 390–400 (1966).
13. G. Boccaletti, R. Ferrari, B. Fox-Kemper, Mixed layer instabilities and restratification. *J. Phys. Oceanogr.* **37**, 2228–2250 (2007).
14. I. N. James, L. J. Gray, Concerning the effect of surface drag on the circulation of a baroclinic planetary atmosphere. *Q. J. R. Meteorol. Soc.* **112**, 1231–1250 (1986).
15. N. Nakamura, Two-dimensional mixing, edge formation, and permeability diagnosed in an area coordinate. *J. Atmos. Sci.* **53**, 1524–1537 (1996).
16. J. Marshall, E. Shuckburgh, H. Jones, C. Hill, Estimates and implications of surface eddy diffusivity in the Southern Ocean derived from tracer transport. *J. Phys. Oceanogr.* **36**, 1806–1821 (2006).
17. A. Mahadevan, A. Tandon, An analysis of mechanisms for submesoscale vertical motion at ocean fronts. *Ocean Model.* **14**, 241–256 (2006).
18. X. Capet, J. C. McWilliams, M. J. Molemaker, A. Shchepetkin, Mesoscale to submesoscale transition in the California current system. Part I: Flow structure, eddy flux, and observational tests. *J. Phys. Oceanogr.* **38**, 29–43 (2008).
19. L. Brannigan, Intense submesoscale upwelling in anticyclonic eddies. *Geophys. Res. Lett.* **43**, 3360–3369 (2016).
20. S. D. Bachman, J. R. Taylor, K. A. Adams, P. J. Hosegood, Mesoscale and submesoscale effects on mixed layer depth in the Southern Ocean. *J. Phys. Oceanogr.* **47**, 2173–2188 (2017).
21. I. Cerovečki, L. D. Talley, M. R. Mazloff, G. Maze, Subantarctic mode water formation, destruction, and export in the eddy-permitting Southern Ocean state estimate. *J. Phys. Oceanogr.* **43**, 1485–1511 (2013).
22. J.-B. Sallée, R. J. Matear, S. R. Rintoul, A. Lenton, Localized subduction of anthropogenic carbon dioxide in the Southern Hemisphere oceans. *Nat. Geosci.* **5**, 579–584 (2012).
23. A. C. N. Garabato, R. Ferrari, K. L. Polzin, Eddy stirring in the Southern Ocean. *J. Geophys. Res. Oceans* **116**, C09019 (2011).
24. E. Shuckburgh, H. Jones, J. Marshall, C. Hill, Understanding the regional variability of eddy diffusivity in the pacific sector of the Southern Ocean. *J. Phys. Oceanogr.* **39**, 2011–2023 (2009).
25. R. Abernathey, J. Marshall, M. Mazloff, E. Shuckburgh, Enhancement of mesoscale eddy stirring at steering levels in the Southern Ocean. *J. Phys. Oceanogr.* **40**, 170–184 (2010).
26. M. Lévy, R. Ferrari, P. J. S. Franks, A. P. Martin, P. Rivière, Bringing physics to life at the submesoscale. *Geophys. Res. Lett.* **39**, L14602 (2012).
27. A. Mahadevan, The impact of submesoscale physics on primary productivity of plankton. *Annu. Rev. Mar. Sci.* **8**, 161–184 (2016).
28. J. R. Taylor, R. Ferrari, Ocean fronts trigger high latitude phytoplankton blooms. *Geophys. Res. Lett.* **38**, L23601 (2011).
29. A. Mahadevan, E. D'Asaro, C. Lee, M. J. Perry, Eddy-driven stratification initiates North Atlantic spring phytoplankton blooms. *Science* **337**, 54–58 (2012).
30. J. R. Taylor, Turbulent mixing, restratification, and phytoplankton growth at a submesoscale eddy. *Geophys. Res. Lett.* **43**, 5784–5792 (2016).
31. J. K. Moore, M. R. Abbott, Phytoplankton chlorophyll distributions and primary production in the Southern Ocean. *J. Geophys. Res.* **105** 28709–28722 (2000).
32. T. N. Lee, J. A. Yoder, L. P. Atkinson, Gulf Stream frontal eddy influence on productivity of the southeast us continental shelf. *J. Geophys. Res. Oceans* **96**, 22191–22205 (1991).
33. J. R. Taylor, *Numerical Simulations of the Stratified Oceanic Bottom Boundary Layer* (University of California, San Diego, 2008).
34. G. E. Karniadakis, M. Israeli, S. A. Orszag, High-order splitting methods for the incompressible Navier-Stokes equations. *J. Comput. Phys.* **97**, 414–443 (1991).
35. S. A. Orszag, Numerical simulation of incompressible flows within simple boundaries. I. Galerkin (spectral) representations. *Stud. Appl. Math.* **50**, 293–327 (1971).
36. W. G. Large, S. Pond, Open ocean momentum flux measurements in moderate to strong winds. *J. Phys. Oceanogr.* **11**, 324–336 (1981).
37. J. R. Taylor, R. Ferrari, Buoyancy and wind-driven convection at mixed layer density fronts. *J. Phys. Oceanogr.* **40**, 1222–1242 (2010).
38. L. N. Thomas, J. R. Taylor, R. Ferrari, T. M. Joyce, Symmetric instability in the Gulf Stream. *Deep-Sea Res. II Top. Stud. Oceanogr.* **91**, 96–110 (2013).
39. J. B. Sallée, K. Speer, R. Morrow, Response of the Antarctic Circumpolar Current to atmospheric variability. *J. Climate* **21**, 3020–3039 (2008).
40. V. Pellichero, J.-B. Sallée, S. Schmidtko, F. Roquet, J.-B. Charrassin, The ocean mixed-layer under Southern Ocean sea-ice: Seasonal cycle and forcing. *J. Geophys. Res.* **122**, 1608–1633 (2016).
41. J. C. McWilliams, Submesoscale currents in the ocean. *Proc. R. Soc. A* **472**, 20160117 (2016).

Acknowledgments: We thank three anonymous reviewers for helpful comments and suggestions. Data collection and technical support were received from the British Antarctic Survey, the crew of *RRS James Clark Ross*, and the NERC Earth Observation and Data Acquisition and Analysis Service (NEODAAS) and Plymouth Marine Laboratory (PML) remote sensing groups. Seasoar and MVP operations were led by National Marine Facilities technicians P. Provost, D. Mountifield, J. Wood, and C. Cameron from the UK National Oceanographic Centre. **Funding:** This work was funded through the National Environmental Research Council (standard grants NE/J010472/1 and NE/J009857/1). **Author contributions:** J.R.T. ran the numerical simulations, conducted the linear stability analysis, and wrote the first draft of the paper. K.A. processed the collected observations and made Fig. 1. K.A. and J.-B.S. helped calculate the global subduction estimate. P.H. was the chief scientist on JR311 and the principal investigator of SMILES. All authors participated in discussions of the results, helped revise the text, and contributed to the collection of observational data. **Competing interests:** The authors declare that they have no competing interests. **Data and materials availability:** All data needed to evaluate the conclusions in the paper are present in the paper and/or the Supplementary Materials and available from www.repository.cam.ac.uk and www.bodc.ac.uk. Additional data related to this paper may be requested from the authors.

Submitted 3 July 2017
Accepted 13 February 2018
Published 28 March 2018
10.1126/sciadv.aao2824

Citation: J. R. Taylor, S. Bachman, M. Stamper, P. Hosegood, K. Adams, J.-B. Sallee, R. Torres, Submesoscale Rossby waves on the Antarctic circumpolar current. *Sci. Adv.* **4**, eaao2824 (2018).

Submesoscale Rossby waves on the Antarctic circumpolar current

John R. Taylor, Scott Bachman, Megan Stamper, Phil Hosegood, Katherine Adams, Jean-Baptiste Sallee and Ricardo Torres

Sci Adv **4** (3), eaao2824.
DOI: 10.1126/sciadv.aao2824